The International Journal of Advanced Manufacturing Technology (2019) 103:957–969
https://doi.org/10.1007/s00170-019-03566-9

ORIGINAL ARTICLE

Solidification prediction of laser cladding 316L by the finite element simulation

Pengzhao Ma[1] · Yu Wu[1] · Pengju Zhang[1] · Jingqing Chen[1]

Received: 10 December 2018 / Accepted: 11 March 2019 / Published online: 28 March 2019

Abstract
Laser cladding technology has been widely applied in industrial production because of its prominent advantage in surface modification. To achieve improved microstructure characteristics and performance, it is essential to investigate the solidification mechanism of the microstructures formed during laser cladding. In this study, the columnar-to-equiaxed transition for laser-clad 316L was predicted using a three-dimensional finite element model coupled with electron backscatter diffraction analysis. First, the distribution of thermodynamic variables at different laser powers was examined. Then, the fitting curve for predicting the columnar-to-equiaxed transition was established, and the results indicate that the solidification of laser-clad 316L can be accurately predicted. Moreover, the grain size distribution for different laser powers was counted, and the average grain size of the molten pool was shown to increase with increasing laser power. This work will serve as a guide for the crystal transition in the solidification process for laser cladding.

Keywords Solidification prediction · Columnar-to-equiaxed transition · Laser cladding · 316L

1 Introduction

Laser cladding is a well-known material surface modification technology that is attracting increasingly more attention because it can improve the wear and corrosion resistances of the substrate [1]. Moreover, the bond strength is stronger than that achieved using traditional thermal spraying techniques because of improved metallurgical bonding between the substrate and coating [2]. Laser cladding technology has been gradually introduced into industrial manufacture in recent years [3].

Currently, researchers are increasingly paying attention to the microstructure of the laser-clad layer because the wear and corrosion resistances of the coating are affected by the microstructure. Wang et al. [4] observed that Ni60 cladding layers to which 4% CeO_2, 5% Y_2O_3, and 5% La_2O_3 were added were superior to those without the rare-earth oxides, as the former displayed compact dendritic structures and more refined grains. Sun et al. [5] investigated the microstructural evolution mechanism of Ni45/NbC composite cladding using scanning electron microscopy (SEM) and calculations and concluded that the microscopic morphology was affected by the atom distribution, temperature gradient, and solidification rates. Zhou et al. [6] reported that the properties on top of a remelting coating were preferable compared with those on top of a cladding coating because of the more refined microstructure. Adesina et al. [7] observed that the wear resistance of coatings with different proportions of CP-Ti and Co powders deposited was improved; they attributed this improvement to the presence of flower-like structures and hard intermetallic phases of $CoTi_2$, CoTi, $AlTi_2$, $AlCo_5$, $AlCo_2Ti$, and Al_2Ti. Jiao et al. [8] fabricated T15M cladding coatings on a Q235 substrate surface using different laser scanning speeds. Electron probe microanalysis confirmed that the amount of carbide precipitates in the original austenite grain boundary increased with increasing laser scanning speed.

Recently, research interests have been extended to the prediction of the solidification of the molten pool such as

✉ Jingqing Chen
simweld@163.com

Pengzhao Ma
mifanjun530@163.com

Yu Wu
m18349261985@163.com

Pengju Zhang
793464033@qq.com

[1] Southwest Jiao Tong University, Chengdu, China

Table 1 Chemical compositions of AISI 304 stainless steel and 316L powder (wt/%)

	Cr	Ni	Si	C	Mn	P	Mo	Fe
AISI304	18.0~20.0	8.0~10.0	≦ 1.0	≦ 0.08	≦ 2.0	≦ 0.045	–	Balance
316L	16.8	13.8	0.75	0.03	0.3	–	2.2	Balance

the columnar-to-equiaxed transition (CET) in additive manufacturing (AM). Many thermodynamic variables such as the temperature gradient, cooling rate, and solidification rate have been shown to affect the solidification of the molten pool [9]. As laser cladding is a fairly complex non-equilibrium thermodynamic process, it is difficult to accurately control these variables experimentally [10]. Numerical simulation is a powerful tool for understanding grain growth, and a number of numerical simulation models have been established. Song et al. [11] established a numerical simulation model to predict the free surface curvature and dimensions of the molten pool considering the effect of the interaction between the powder jets and observed an agreement between the predicted thermal gradient directions and grain growth orientations. Yang et al. [12] explored a two-dimensional cellular automata (CA) model to simulate the processes of solidification and solid-state phase transformation in selective laser melting (SLM). The topography and size of the grain were primarily anastomosed with the simulation. Liu et al. [13] developed a quantitative semi-empirical method coupled with the molten pool prediction using the Rosenthal solution to determine the relationship between the microstructure and process parameters of the metal SLM process. Botello et al. [14] integrated a two-dimensional CA model with finite-element (FE) simulation (CA-FE) to predict the microstructure of the powder additive AA2024 during the SLM process. Most of the above models are based on a CA or CA-FE model. Model building for the CA method requires a profound theoretical foundation and complex mathematical models, which is fairly complicated. Because of the advantages of modules and currency, FE simulation is the ideal tool for predicting microstructure transition.

Literature on the prediction of microstructural transitions in AM using only FE tools is scarce. Liu et al. [15] established the criterion for the CET using a three-dimensional (3D) FE model and observed that the morphologies of the molten pool and track surface coincided well with the simulation results. In the present work, a 3D FE model that shows good agreement with the molten transverse topography and thermal cycle was developed and combined with the CET theory to predict the microstructures of a single-track laser cladding layer of 316L. In addition, it was verified that the fitting curve obtained from the simulation accurately predicted the transformation of columnar into equiaxed crystals.

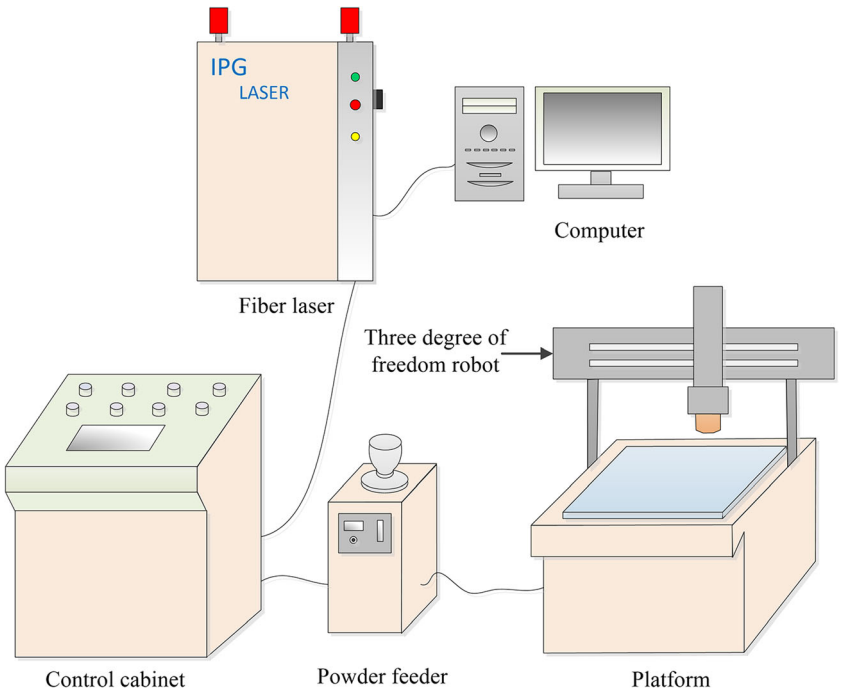

Fig. 1 Schematic diagram of laser cladding system

Table 2 Process parameters for laser cladding

Sample	Laser power (w)	Scanning speed (mm/min)	Shielding gas (L/min)
1	1000	160	30
2	1200	160	30
3	1300	160	30

2 Experiment

2.1 Material and equipment

77The nominal compositions of the 316L powder and 304 austenite stainless steel are shown in Table 1. The diameter of the spherical 316L particles is in the range of 50–120 μm. Figure 1 presents a schematic diagram of laser cladding system. The cladding layers were fabricated using a YLS-4000 fiber laser installed in a three-axis robot with a laser wavelength of 1.06 μm and spot diameter of 3 mm. A cabinet was used to control the laser power, and a computer interface was used to program the scanning strategy and scanning speed. High-purity argon (99.999%) served as a shielding gas to protect the molten pool from oxidation during the laser-cladding process. A mixture of erosion solution (3 g $CuCl_2$, 50 mL of HCl, and 50 mL of ethanol) was used to etch the samples to examine transverse cross-sections of the molten pool.

2.2 Experimental procedure

Before the experiment, the 316L powder was dried in a drying furnace at 120 °C for 1 h to remove the water, and the substrate was ground by a grinding machine to remove the rust. The cladding process parameters in this study are presented in Table 2. A schematic diagram of the molten pool formation with the laser beam moving is presented in Fig. 2. The metal powder from the power tube with the protection of high-purity argon was melted under the action of the laser heat source on the substrate surface. A K-type thermocouple was used to determine the temperature at a point approximately 3 mm away from the cladding layer. Thereafter, transverse cross-sections of the molten pools were examined using an optical microscope. In addition, the microstructures of the cladding layers were analyzed using electron backscattered diffraction (EBSD) with a step size of 1 μm.

3 FE model of laser cladding

3.1 Physical model

A 3D FE model (Fig. 3) was established using the commercial software ABAQUS. The geometrical dimensions of the substrate are 650 × 40 × 10 mm^3, and the length of the cladding layer is 500 mm. Considering the calculation precision and efficiency, the quantity and quality of the mesh were optimized. The areas around the cladding layer were fine meshed with a size of approximately 0.2 mm. In the other parts of the

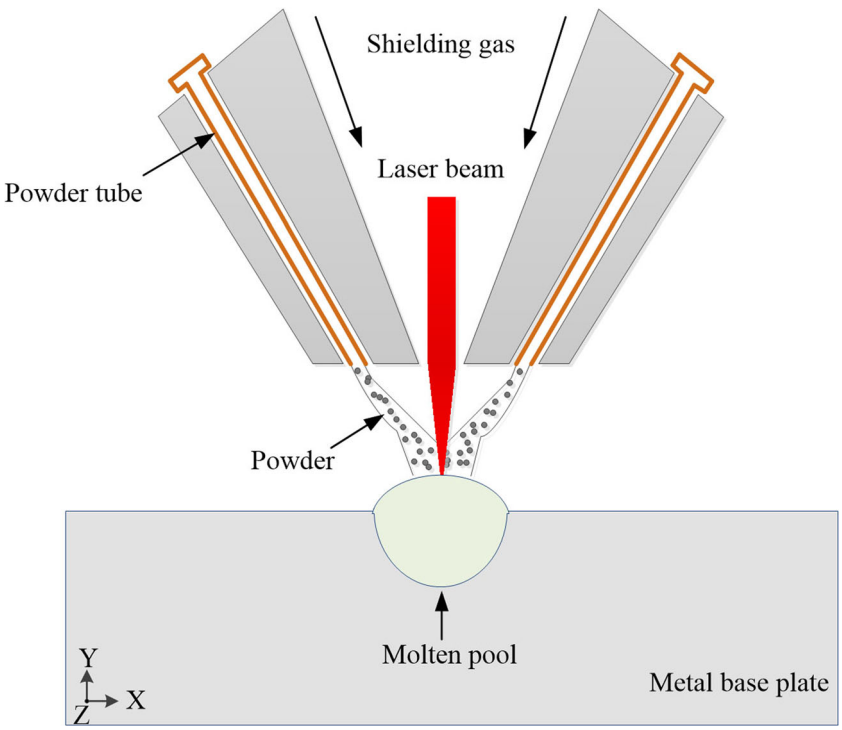

Fig. 2 Schematic diagram of molten pool formation

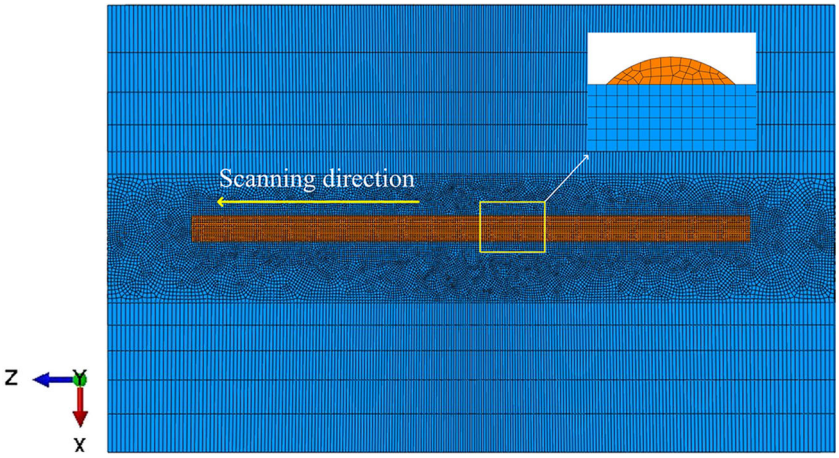

Fig. 3 3D physical model (top view)

model, the mesh size was gradually increased from the cladding layer to the substrate. The material property parameters of 316L and 304 stainless steel (as shown in Table 3) changed with temperature during laser cladding [16].

3.2 Governing equations and boundary conditions

When a laser beam irradiates a powder, a small amount of the laser energy is absorbed by the powder particles and the substrate and most of the energy is reflected. The temporal and spatial components of the temperature distribution are governed by the 3D nonlinear transient heat conduction governing equation [17]:

$$\rho c\frac{\partial T}{\partial t}=\frac{\partial}{\partial x}\left(k_{xx}\frac{\partial T}{\partial x}\right)+\frac{\partial}{\partial y}\left(k_{yy}\frac{\partial T}{\partial y}\right)+\frac{\partial}{\partial z}\left(k_{zz}\frac{\partial T}{\partial z}\right)+\phi \tag{1}$$

where ρ is the material density; c is the specific heat capacity; k_{xx}, k_{yy}, and k_{zz} are the thermal conductivity in the x-, y-, and z-

Table 3 Material property parameters of 316L and AISI304

Temperature	Thermal conductivity		Specific heat capacity		Density	
°C	W/(m k)		J/(g k)		0.01 g/mm^3	
	316L	AISI304	316L	AISI304	316L	AISI304
20	14.0	14.8	0.497	0.564	0.777	0.800
100	15.3	15.9	0.519	0.570	0.773	0.791
200	17.5	17.3	0.544	0.577	0.768	0.783
500	22.0	21.2	0.585	0.600	0.755	0.781
800	25.6	25	0.614	0.627	0.741	0.771
1000	29.2	27.6	0.678	0.645	0.733	0.763
1200	32.1	29.5	0.742	0.662	0.741	0.756
1400	28.4	31.4	0.806	0.679	0.777	0.753

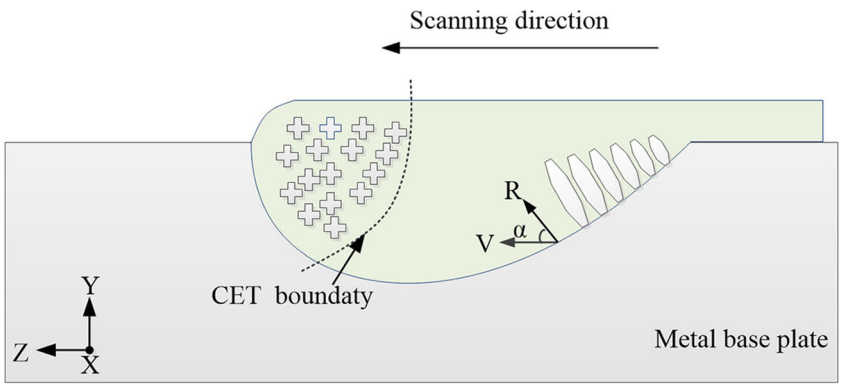

Fig. 4 Schematic illustration of columnar-to-equiaxed transition

axis directions, respectively; and ϕ is the heat generated per unit volume.

The convection boundary conditions and radiation boundary conditions on the outer surface of the substrate are considered to be

$$\theta = \theta_0 + \varepsilon\sigma(T-T_0)(T+T_0)^2 \quad (2)$$

where θ is the convective and radiative heat transfer coefficient; θ_0 is the convective heat transfer coefficient at room temperature; and ε and σ are the radiant coefficient and Boltzmann's constant, respectively. The initial temperature (T_0) was considered to be 28 °C.

3.3 Heat source model

Laser cladding is equivalent to a heat treatment process with rapid heating and cooling in a local region. With the movement of the heat source, the temperature of the entire workpiece changes rapidly with time and space. To achieve good agreement with the transverse cross-section of the molten pool, a hybrid heat source model composed of a Gaussian body heat source model and Gaussian area heat source was established.

The Gaussian body heat source model distribution can be expressed by the following equation:

$$q_1(r,z) = \frac{6f_1Q}{\pi R_1 H(mH+2D_1)}\exp\left(\frac{-3r^2}{D_1^2}\right)\left(\frac{mh+D_1}{D_1}\right). \quad (3)$$

The Gaussian surface heat source model distribution can be expressed by the following equation:

$$q_2(r,z) = \frac{3f_2Q}{\pi D_2^2}\exp\left(\frac{-3r^2}{D_2^2}\right). \quad (4)$$

Here, Q is the effective laser power; r is the distance between an arbitrary node and the center; D_1 and D_2 are the effective radii of the heat source; h is the height of the heat source at any cross-section; H is the effective depth of the heat source; m is the linear attenuation coefficient; f_1 and f_2 are the heat distribution function of the Gaussian body heat source and Gaussian area heat source, respectively; and $f_1 + f_2 = 1$.

3.4 Criterion for columnar-to-equiaxed transition

Liu et al. [15] proposed a criterion based on the G^n/V ratio that the microstructure will be columnar when G^n/V is greater than a critical value; otherwise, the microstructure will be equiaxed. A simplified model of the growth of columnar and equiaxed grains as well as the CET boundary between the two types of grains is presented in Fig. 4. V is the scanning speed, and R is the solidification rate, which is determined by the speed of laser scanning and the shape of molten pool.

$$R = V\cos\alpha \quad (5)$$

Here, α is the angle between R and V. When $\alpha = 0°$, R is the maximum solidification rate, and its value is equal to the scanning speed.

R is calculated using Eq. (6).

$$R = V_n/G \quad (6)$$

where V_n is the cooling rate and G is the temperature gradient.

$$G = q/\lambda \quad (7)$$

Here, q is the heat flux, which can be obtained from a subroutine of GETVRM, and λ is the thermal conductivity.

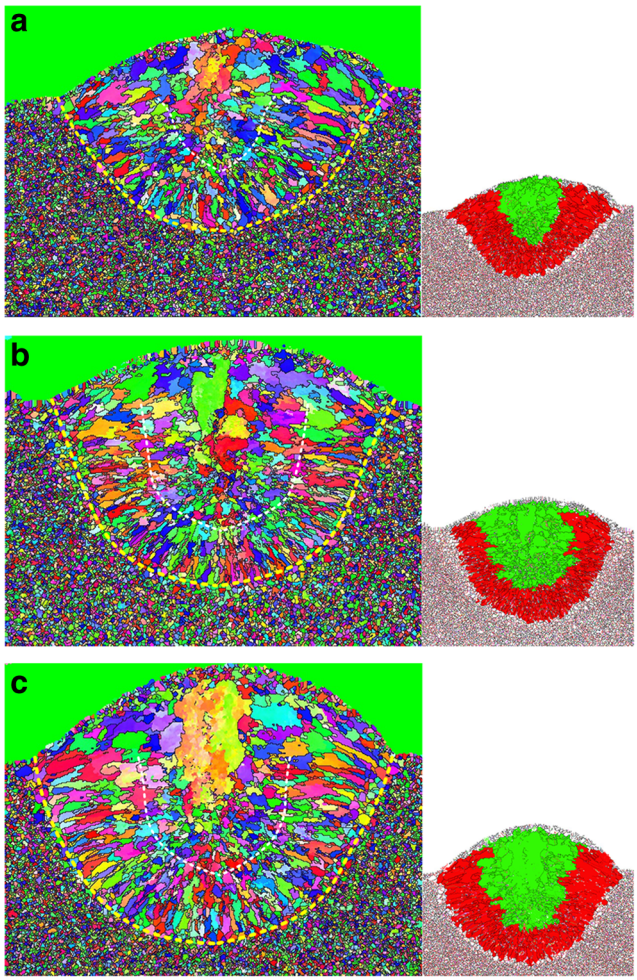

Fig. 5 IPF maps for different laser powers. **a** P=1000 W, **b** P=1200 W, **c** P=1300 W

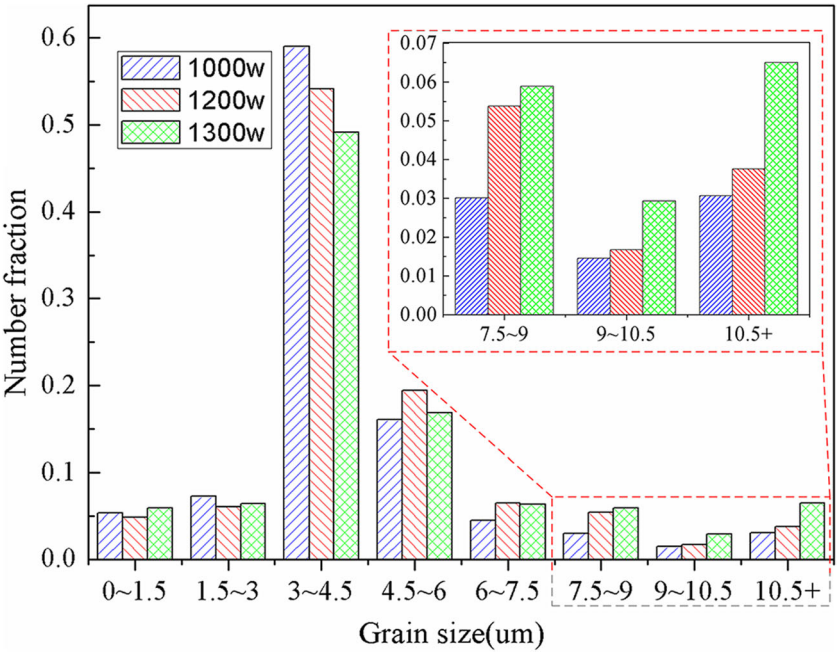

Fig. 6 Grain size distribution for different laser powers

4 Results and discussion

4.1 Microstructure of cladding layers

The microstructures of the cladding layers for different laser powers are presented in Fig. 5. The microstructures of the cladding layer and base metal are completely austenite. Hadadzadeh et al. [18] presented a criterion for identifying columnar and equiaxed crystals related to the grain shape aspect ratio Φ. The grains are considered to be elliptical, with long axis L_1 and short axis L_2. If $\Phi \leq 0.33$ ($\Phi = L_2{:}L_1$), the grains are regarded as columnar; otherwise, they are regarded as equiaxed. Using this criterion, the equiaxed crystals were colored green, and the columnar crystals were colored red (Fig. 5). Surrounded by the yellow dashed line and the white dashed line are the molten pool zones and the boundary between the columnar and equiaxed grains, respectively.

Figure 6 shows the grain size distribution for different laser powers; the grain size is concentrated in the range of 3–6 μm. With increasing laser power, the fraction of grains with sizes > 7.5 μm, and especially those with sizes > 10.5 μm, gradually increased. The average grain sizes of the molten pool at powers of 1000, 1200, and 1300 W were calculated to be 4.99, 5.25, and 5.65 μm, respectively. These results suggest that the

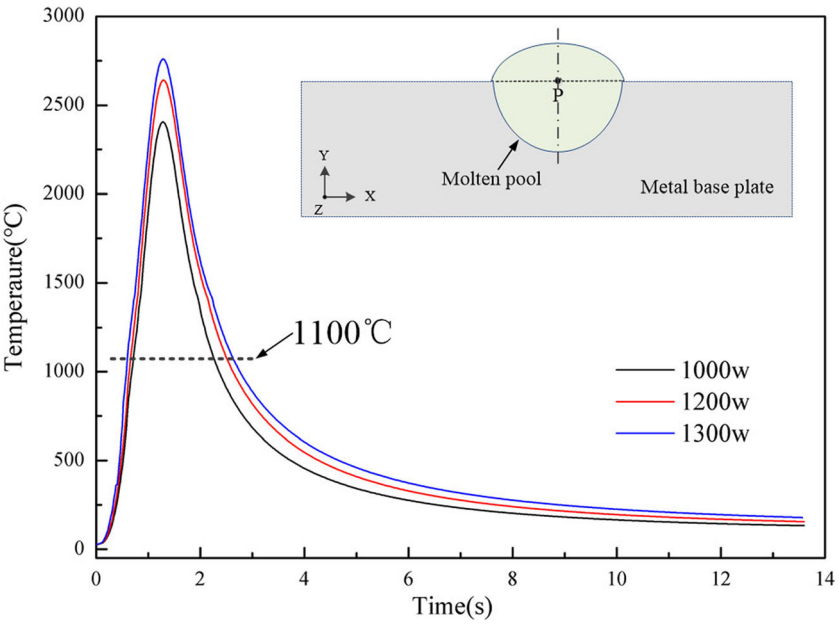

Fig. 7 Thermal cycle for different laser powers

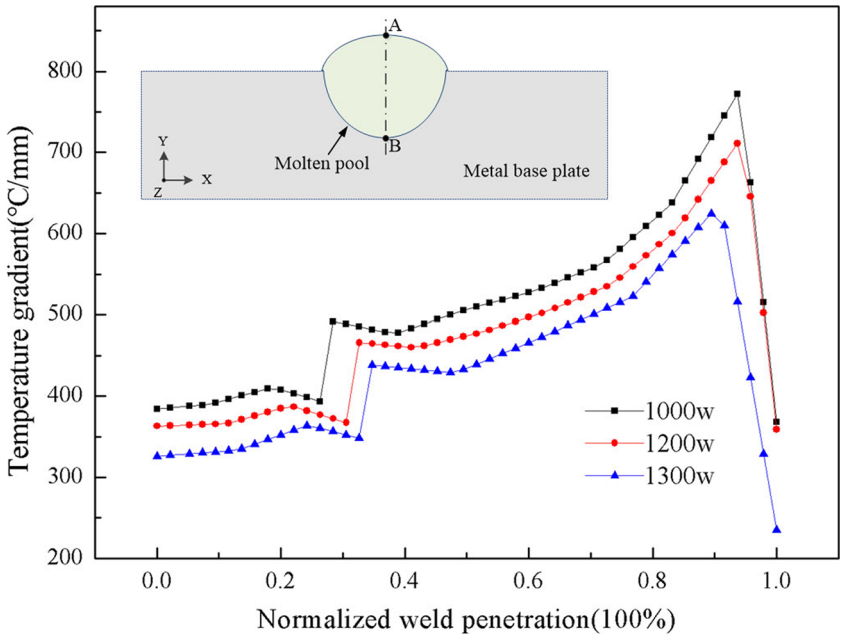

Fig. 8 Temperature gradient for different laser powers

average grain size of the molten pool increases with increasing laser power.

The simulated thermal cycle of one marked point and the simulated temperature gradient of segment AB, which represents the distance from the top to the bottom of the pool, for different laser power in the cladding layer are shown in Figs. 7 and 8, respectively. The austenite grains of stainless steel will grow from the peak temperature to approximately 1100 °C. The peak temperature and time in the high-temperature region shown in Fig. 7 and the temperature gradient shown in Fig. 8 increased with increasing laser power, which would result in an increase in the average grain size.

The components of the laser cladding were identified using energy-dispersive X-ray spectroscopy (EDS). The line scan results of segment AB are presented in Fig. 9. The EDS spectra confirm the presence of 0.63 wt% Mo. Therefore, the fabricated cladding layer improves the corrosion resistance of the substrate [19].

4.2 Validation of temperature field

To verify the accuracy of the FE model based on ABAQUS, the thermal cycle of a feature point was measured using a K-

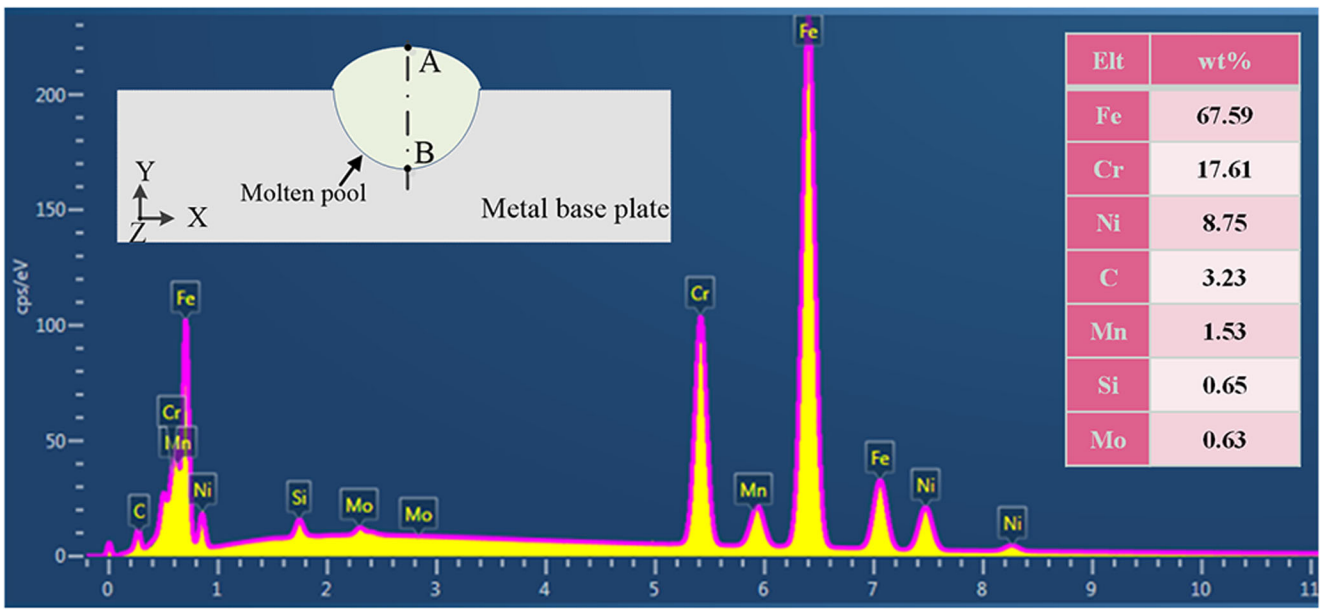

Fig. 9 EDS analysis of laser cladding

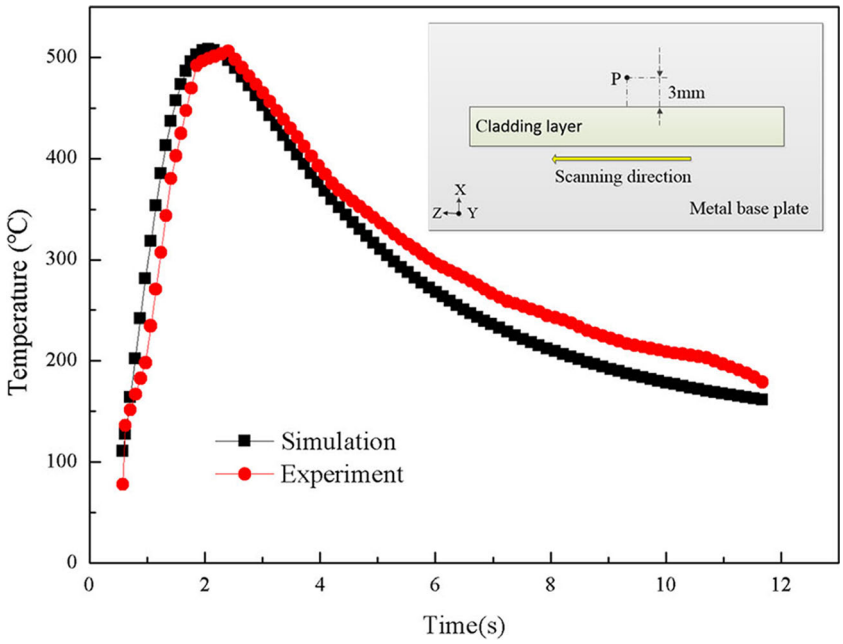

Fig. 10 Comparison between measured and simulated thermal cycle curves

type thermocouple. As observed in Fig. 10, the results of the simulated thermal cycle curve were compared with the measured curve. Overall, the simulated and experimental results generally showed good agreement. The comparison verified the reliability and accuracy of the FE model.

Through the calculation of the temperature field, the simulated transverse cross-sections of the molten pool were compared with the experimental results, as shown in Fig. 11. The simulated results were in good agreement with the experimental results.

4.3 Simulation results for thermodynamic variables

The distribution of thermodynamic variables including the cooling rate (V_n), temperature gradient (G), and solidification rate (R) in the molten pool was analyzed. The simulation

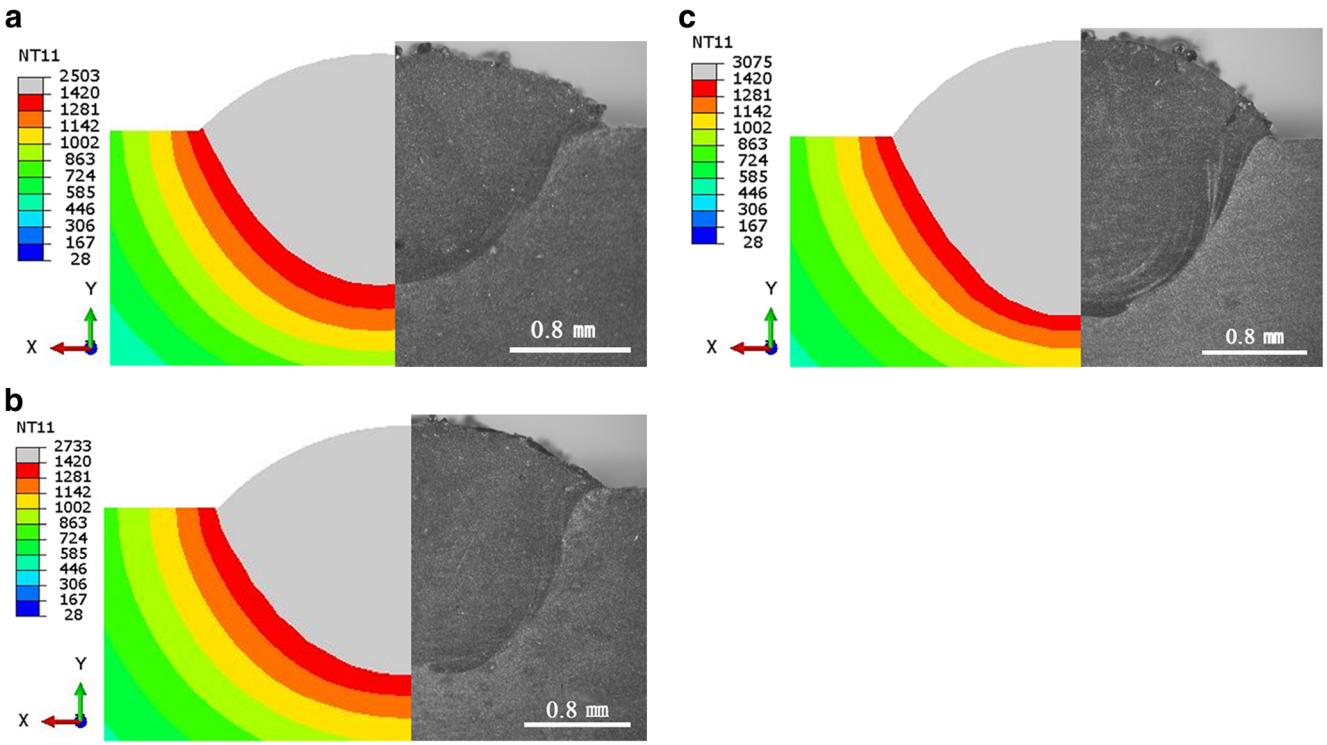

Fig. 11 Comparison of simulated transverse cross-sections of molten pool and experimental results. **a** P=1000 W, **b** P=1200 W, **c** P=1300 W

results are presented in Figs. 12, 13, and 14, and the black dashed lines represent the profile of the molten pool.

Taken together, it can be observed that increasing laser power, the maximum value of these thermodynamic variables gradually decreased.

The observed results can be explained using the Rosenthal 3D equation:

$$\frac{2\pi(T-T_0)kr}{Q} = \exp\frac{-V(r-z)}{2\beta}, \tag{8}$$

where k is the thermal conductivity, r is the distance between an arbitrary node and the center, Q is the effective laser power, V is the scanning speed, β is the thermal diffusivity, and z is scanning direction. In this study, the value of V was 160 mm/min. As shown in Fig. 3, the scanning direction is along the z-axis. If we consider the temperature along the scanning direction, such that

$$x = y = 0; r = z, \tag{9}$$

and we substitute Eq. (9) into Eq. (8), we obtain

$$T-T_0 = \frac{Q}{2\pi kz}. \tag{10}$$

The temperature gradient can be expressed as

$$\left(\frac{\partial T}{\partial z}\right)_t = \frac{Q}{2\pi k} \times \left(-\frac{1}{z^2}\right) = -2\pi k\frac{(T-T_0)^2}{Q}. \tag{11}$$

And, the cooling rate can be expressed as

$$\left(\frac{\partial T}{\partial t}\right)_z = \left(\frac{\partial T}{\partial z}\right)_t \left(\frac{\partial z}{\partial t}\right)_T = -2\pi kV\frac{(T-T_0)^2}{Q}. \tag{12}$$

From Eqs. (11) and (12), it can be deduced that the temperature gradient and cooling rate both decrease with increasing effective laser power. Therefore, with increasing laser power, the maximum value of the thermodynamic variables gradually decreased.

As observed in Fig. 12a, Fig. 13a, and Fig. 14a, the maximum value of the cooling rate is distributed in the middle and lower parts of the molten pool. As illustrated in Fig. 12b, Fig. 13b, and Fig. 14b, the maximum value of the temperature gradient is distributed at the bottom of the molten pool, and the minimum value is distributed at the top of the molten pool; these findings are similar to those reported by Zhang et al. [20]. In addition, the temperature gradient at the edge of the molten pool gradually decreases from the edge to the center. Figure 12c, Fig. 13c, and Fig. 14c show that the maximum

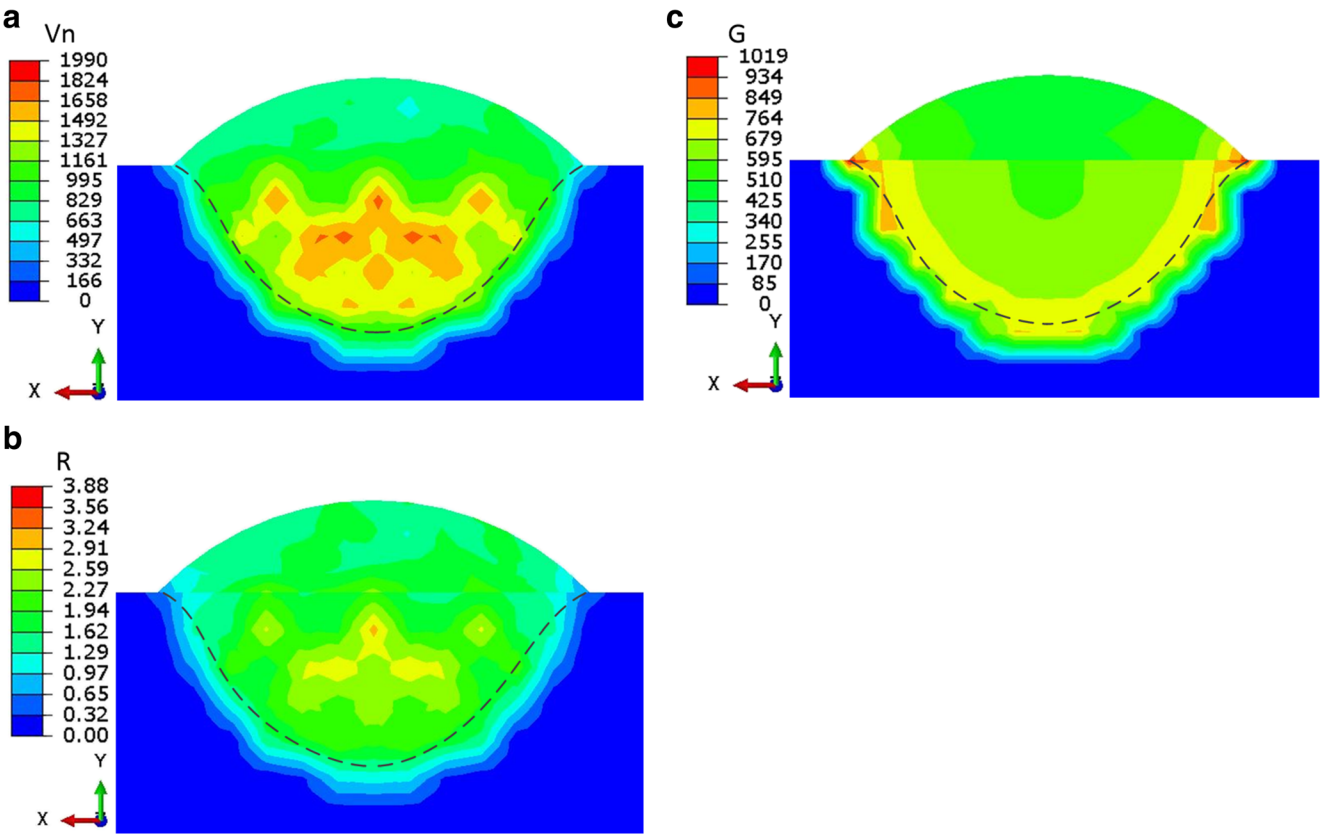

Fig. 12 Simulation results for thermodynamic variables for sample 1 ($P = 1000$ W). **a** Cooling rate, **b** Temperature gradient, **c** Solidification rate

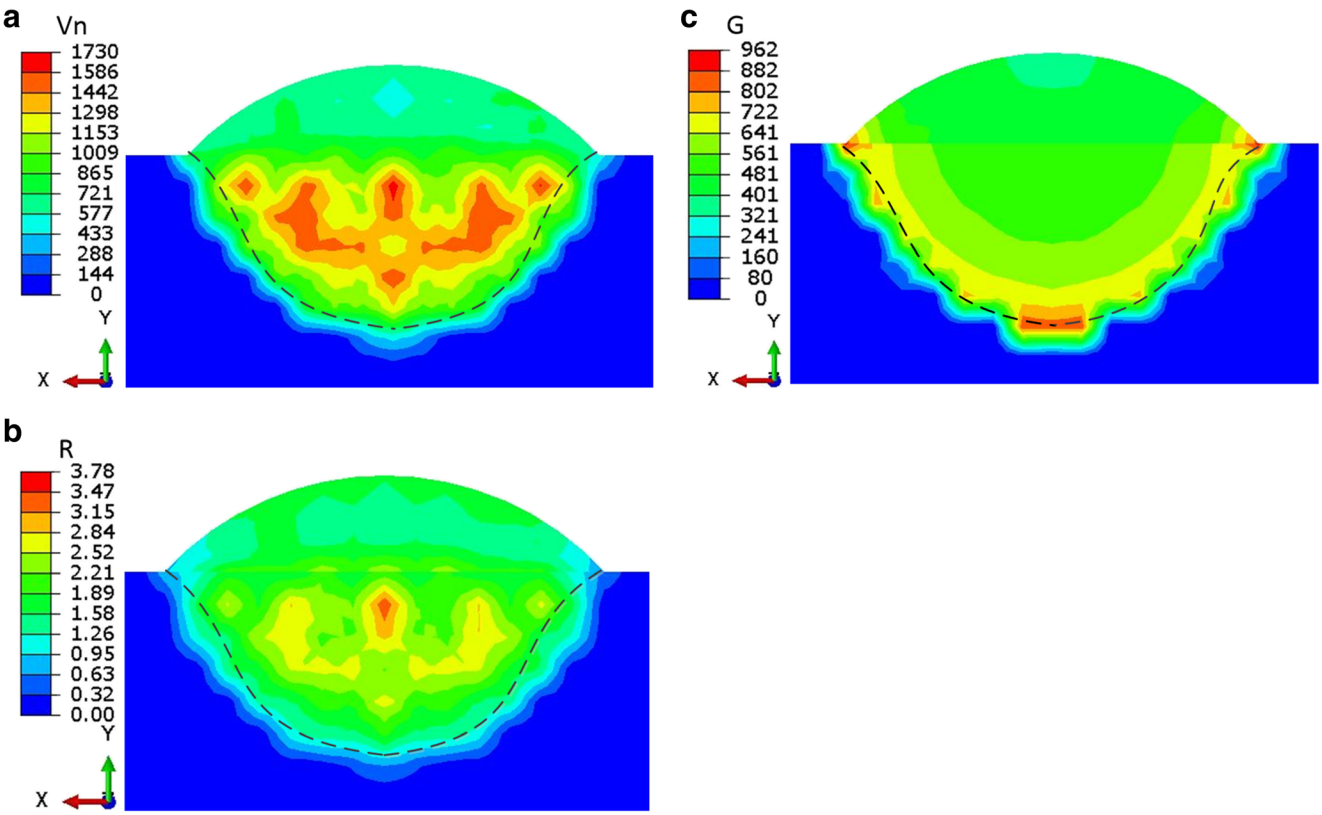

Fig. 13 Simulation results for thermodynamic variables for sample 2 ($P = 1200$ W). **a** Cooling rate, **b** Temperature gradient, **c** Solidification rate

solidification rate appears in the center of the molten pool and that the minimum value appears at the edge of the molten pool, which presents an opposite trend to the temperature gradient.

During the solidification process, the internal heat dissipation of the molten pool is slower, whereas that of the bottom part of the molten pool is faster because of thermal conduction via the substrate or former solidified layers. Therefore, the temperature gradient at the bottom of the molten pool is large. When the molten pool around the fusion line begins to solidify, the cooling rate of the molten pool around the fusion line is relatively slow because of the effect of heat accumulation and heat-source heating. When the solidification proceeds to the middle of the molten pool, the heat source is away from this area, and the effect of the heat-source heating gradually becomes weaker. Therefore, the cooling rate in the middle of the molten pool is the largest. Equation (6) shows that the distributions of the solidification rate and cooling rate are similar.

4.4 Establishment of CET criterion

Carter et al. [21] observed that when the solidification of the molten pool stretches from the bottom to the center, columnar grains form earlier than the equiaxed grains, the columnar grain grows along the molten pool edge to the center of the molten pool until the equiaxed grain in the center of the pool forms, namely the CET. The temperature gradient and solidification rate of the node in Fig. 15 were extracted from the simulation results for the thermodynamic variables. Because the results are symmetric, only half of them are presented in Table 4.

Liu et al. [20] reported that the relationship between G and R fundamentally determines the solidification grain shape. That is, the CET will occur if $G^n/R = C_{st}$; otherwise, equiaxed grains will be present if $G^n/R < C_{st}$; otherwise, columnar grains will be present. Here, C_{st} is the criterion of the CET line and n is the power exponent of G. Combining these relationships with the IPF maps for samples 1 and 2, the temperature gradient and solidification rate of the boundary between the columnar and equiaxed grains were extracted to obtain a fitting curve for the CET. The fitting curve based on Gaussian fitting is presented in Fig. 16. The fitting curve can be used to predict the grain shape in the molten pool of laser cladding.

Sample 3 was used to validate the accuracy of the fitting curve of the CET, and the numerical simulation result is presented in Fig. 17. Based on the user-defined custom colors, the green, red, and blue areas represent

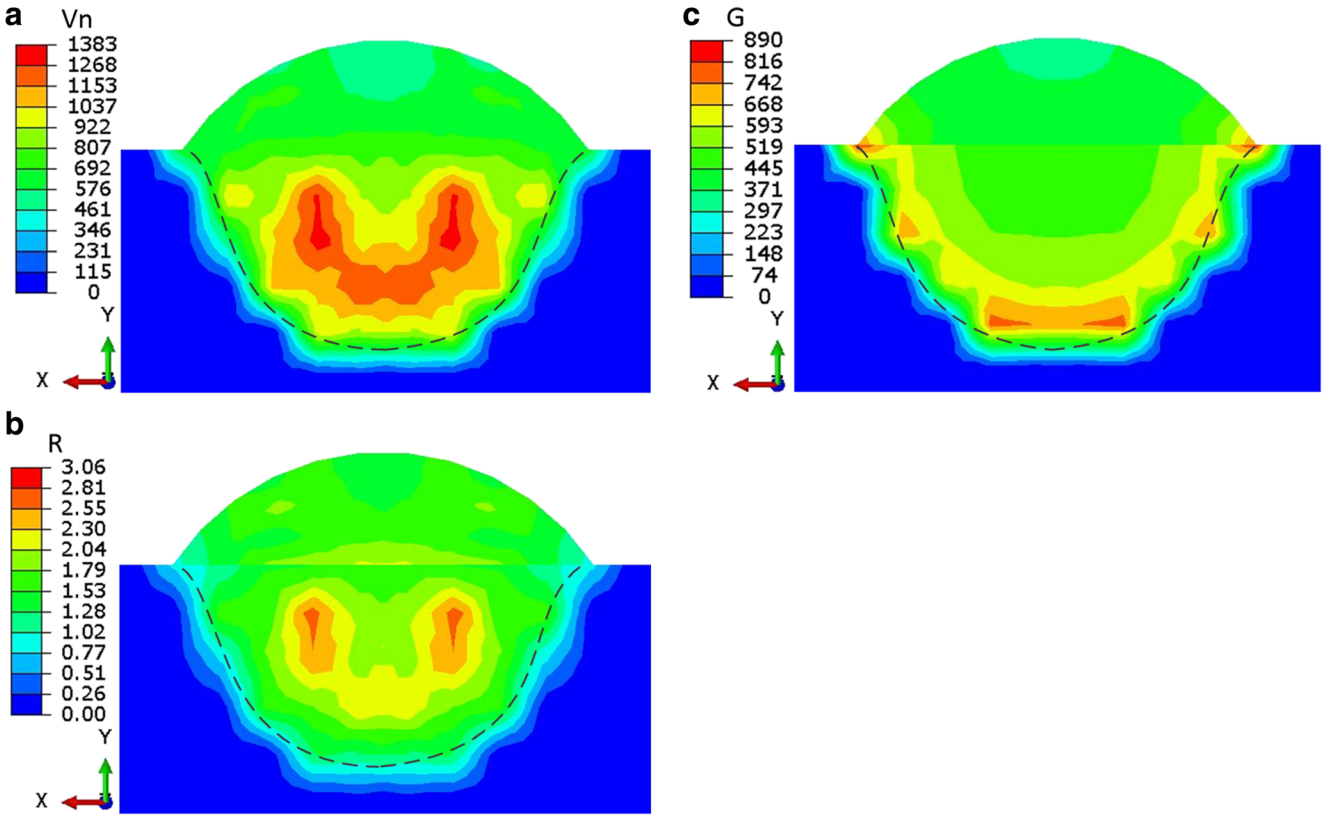

Fig. 14 Simulation results for thermodynamic variables for sample 3 ($P = 1300$ W). **a** Cooling rate, **b** Temperature gradient, **c** Solidification rate

the equiaxed grain, columnar grain, and substrate, respectively. The prediction obtained using the numerical simulation shows good agreement with the experimental grain shape.

5 Conclusions

From the current study, the following main results were observed.

(1) A 3D FE model was established, and the thermal cycle and transverse cross-sections of the molten pool of the FE simulation were in good agreement with the experimental results.

(2) The grain size for different laser powers was concentrated in the range of 3–6 μm, and the average grain sizes were 4.99 μm ($P = 1000$ W), 5.25 μm ($P = 1200$ W), and 5.65 μm ($P = 1300$ W). With increasing laser power, the average grain size and fraction of grains with sizes > 7.5 μm, and especially those > 10.5 μm, gradually increased.

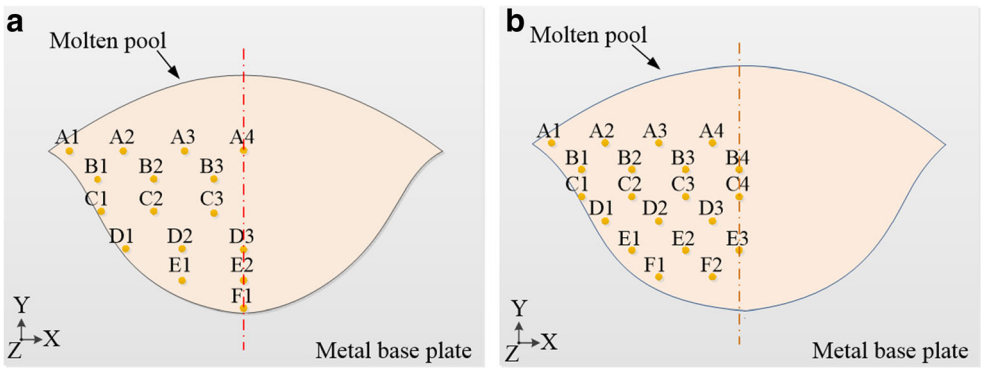

Fig. 15 Schematic diagrams showing different nodes used. **a** P=1000 W, **b** P=1200 W

Table 4 Thermodynamic variables for different nodes

1000 w	A1	A2	A3	A4	B1	B2	B3	C1		
R (mm/s)	0.66	1.66	1.56	1.93	1.26	3.12	1.77	0.74		
G (°C/mm)	8.95	5.64	6.03	5.59	7.74	6.18	5.48	8.13		
1000 w	C2	C3	D1	D2	D3	E1	E2	F1		
R (mm/s)	1.61	2.82	1.26	2.34	3.07	2.09	1.93	1.20		
G (°C/mm)	6.62	6.02	7.50	6.55	6.20	7.00	6.75	7.55		
1200 w	A1	A2	A3	A4	B1	B2	B3	B4	C1	C2
R (mm/s)	0.71	1.60	1.86	2.03	1.30	1.56	3.37	3.24	1.35	2.13
G (°C/mm)	8.91	5.93	4.29	5.00	7.06	5.66	5.03	4.87	7.29	5.90
1200 w	C3	C4	D1	D2	D3	E1	E2	E3	F1	F2
R (mm/s)	3.04	2.63	1.10	2.26	2.34	0.96	1.66	2.32	1.81	1.66
G (°C/mm)	5.32	5.15	6.29	5.87	5.60	6.92	6.15	5.90	6.78	6.54

(3) The maximum value of the cooling rate was distributed in the middle and lower parts of the molten pool. The maximum value of the temperature gradient was distributed at the bottom of the molten pool, and the minimum value was distributed at the top of the molten pool. The maximum value of the solidification rate appeared at the center of the molten pool, and the minimum value appeared at the edge of the molten pool.

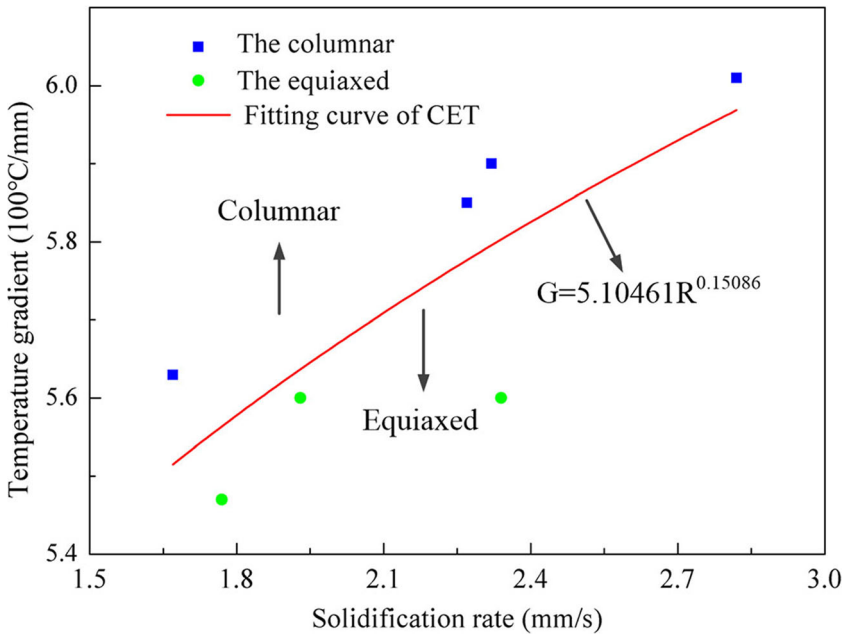

Fig. 16 Fitting curve for CET

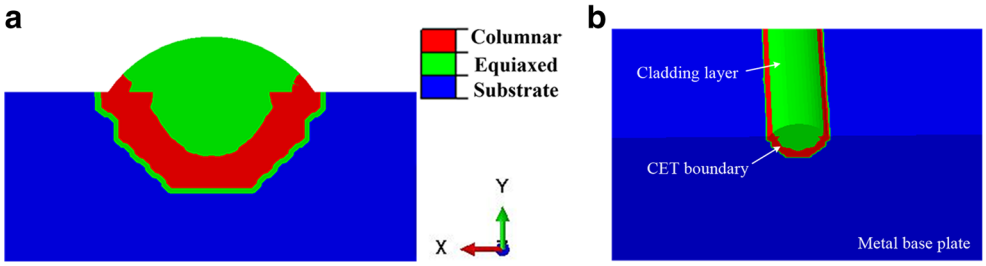

Fig. 17 Validation result for sample 3 ($P = 1300$ W). **a** Transverse cross-section, **b** 3D figure

(4) A fitting curve for the CET was established by connecting the microstructure and thermodynamic variables of the molten pool and was expressed as $G = 5.1046R^{0.15086}$. The verification results indicated that this model can be used to accurately predict the solidification of laser-clad 316L.

Funding information The present study was supported by the National Natural Science Foundation of China (Grant No. 51504198), the National Science Foundation of China (Grant No. 51474178), and the Fundamental Research Funds for the Central Universities (Grant No. A0920502051820-48).

Compliance with ethical standards

Conflict of interest The authors declare that they have no conflict of interest.

References

1. Zhao W, Zha GC, Xi MZ, Gao SY (2018) Effects of synchronous rolling on microstructure, hardness, and wear resistance of laser multilayer cladding. Int J Adv Manuf Technol 27:1746–1752
2. Liu HM, Hu ZQ, Qin XP, Wang YL, Zhang J, Huang S (2017) Parameter optimization and experimental study of the sprocket repairing using laser cladding. Int J Adv Manuf Technol 91:3967–3975
3. Zhao Y, Yu YB, Sun JY, Xi WC, Bi XX (2018) Effect of laser cladding on forming qualities of YCF101 alloy powder in the different lap joint modes. Int J Adv Manuf Technol 96:1991–2001
4. Wang C, Gao Y, Wang R, Wei D, Cai M, Fu Y (2018) Microstructure of laser-clad Ni60 cladding layers added with different amounts of rare-earth oxides on 6063 Al alloys. J Alloys Compd 740:1099–1107
5. Sun S, Fu H, Ping X, Lin J, Lei Y, Wu W (2018) Reinforcing behavior and microstructure evolution of NbC in laser cladded Ni45 coating. Appl Surf Sci 455:160–170
6. Zhou SF, Xu YB, Liao BQ, Sun YJ, Dai XQ (2018) Effect of laser remelting on microstructure and properties of WC reinforced Fe-based amorphous composite coatings by laser cladding. Opt Laser Technol 103:8–16
7. Adesina OS, Popoola API, Pityana SL, Oloruntoba DT (2018) Microstructural and tribological behavior of in situ synthesized Ti/Co coatings on Ti-6Al-4V alloy using laser surface cladding technique. Int J Adv Manuf Technol 95:1265–1280
8. Jiao XY, Wang J, Wang CM, Gong ZQ, Pang XX, Xiong SM (2018) Effect of laser scanning speed on microstructure and wear properties of T15M cladding coating fabricated by laser cladding technology. Opt Lasers Eng 110:163–171
9. Masanta M, Shariff SM, Choudhury AR (2011) Evaluation of modulus of elasticity, nano-hardness and fracture toughness of TiB_2-TiC-Al_2O_3 composite coating developed by SHS and laser cladding. Mater Sci Eng A 528(16–17):5327–5335
10. Casati R, Lemke JN, Vedani M (2016) Microstructure and fracture behavior of 316L austenitic stainless steel produced by selective laser melting. J Mater Sci Technol 32(8):738–744
11. Song J, Chew YX, Bi GJ, Yao XL, Zhang BC (2018) Numerical and experimental study of laser aided additive manufacturing for melt-pool profile and grain orientation analysis. Mater Design 137:286–297
12. Yang JJ, Yu HC, Yang HH, Li FZ, Wang ZM, Zeng XY (2018) Prediction of microstructure in selective laser melted Ti-6Al-4V alloy by cellular automaton. J Alloys Compd 748:281–290
13. Liu J, To AC (2017) Quantitative texture prediction of epitaxial columnar grains in additive manufacturing using selective laser melting. Addit Manuf 16:58–64
14. Botello OL, Hernandez UM, Ramírez J, Pinna C, Mumtaz K (2017) Two-dimensional simulation of grain structure growth within selective laser melted AA-2024. Mater Design 113:369–376
15. Liu SW, Zhu HH, Peng GY, Yin J, Zeng XY (2018) Microstructure prediction of selective laser melting $AlSi_{10}Mg$ using finite element analysis. Mater Design 142:319–328
16. Sabbaghzadeh J, Azizi M, Torkamany MJ (2008) Numerical and experimental investigation of seam welding with a pulsed laser. Opt Laser Technol 40(2):289–296
17. Liu S, Kong F, Shi SH (2014) Study of a hollow laser beam for cladding. Int J Adv Manuf Technol 73:147–159
18. Hadadzadeh A, Amirkhiz BS, Li J, Mohammadi M (2018) Columnar to equiaxed transition during direct metal laser sintering of AlSi10Mg alloy: effect of building direction. Addit Manuf 23:121–131
19. Dong LG, Peng QJ, Han EH, Ke W, Wang L (2018) Microstructure and intergranular stress corrosion cracking susceptibility of a SA508-52M-316L dissimilar metal weld joint in primary water. J Mater Sci Technol 34(8):1281–1292
20. Zhang Z, Farahmand P, Kovacevic R (2016) Laser cladding of 420 stainless steel with molybdenum on mild steel A36 by a high power direct diode laser. Mater Design 109:686–699
21. Carter LN, Martin C, Withers PJ, Attallah MM (2014) The influence of the laser scan strategy on grain structure and cracking behaviour in SLM powder-bed fabricated nickel superalloy. J Alloys Compd 615(2):338–347